HOPF BIFURCATION, VORTEX SHEDDING AND NEAR WAKE STUDY OF A HEATED CYLINDER IN CROSS FLOW[*]

A. SOHANKAR

Dept. of Mech. Eng., Faculty of Engineering, Yazd University, Yazd,I. R. of Iran
Email: asohankar@yazduni.ac.ir

Abstract– The wake flow and the onset of Karman-vortex shedding corresponding to periodic forces of a heated circular cylinder are investigated numerically with a SIMPLEC finite volume code. This study is performed for Reynolds numbers ranging from 20 to 200 and a Prandtl number of 0.7.

The first bifurcation of flow over bluff bodies, which is strictly a Hopf type, is modelled using the Stuart-Landau equation. In this study, it is shown that the flow behind a circular cylinder is steady up to Re=49 and beyond this critical value, the flow develops to a periodic state, corresponding to the vortex shedding and force oscillation on the body. The wake structure is studied close to the oscillation threshold and also at the higher Reynolds numbers using streamlines, pressure, temperature, Nusselt numbers and wall vorticity profiles and iso-lines. Some useful physical quantities, such as time mean separation angle, Nusselt number, the dominating wake frequency (Strouhal and Roshko numbers), mean drag and the RMS value of lift are computed and compared with numerical and experimental results. Based on the results of this study, the empirical relations for the Reynolds dependence of the mean Nusselt number, mean separation angle, Strouhal and Roshko numbers are obtained.

Keywords– Vortex shedding, Hopf bifurcation, heated cylinder, stuart-landau equation, strouhal number, Roshko number, Reynolds number

1. INTRODUCTION

Convective heat transfer between fluid and bluff bodies such as circular cylinders arise in numerous industrial applications like tubular heat exchangers, nuclear reactor fuel rods, boilers, cooling of electronic equipment, chimneys, hot wire anemometry, etc. In spite of the relatively simple geometry of bluff bodies, the flow around these bodies is a complicated flow phenomenon, which has proved a challenging area for researchers in recent years. However, it was not until 1878, when Strouhal published his pioneer paper on singing wires caused by vortex shedding, that this type of flow became a subject of quantitative research. In general, the flow around bluff bodies contains many complex phenomena. The near wake of a bluff body is involved in the interactions between an attached shear layer on the frontal part of the body, the separating free shear layers springing from the sides of the body, and a massive wake flow downstream of the body, each with different and perhaps even coupled processes of developing instabilities as the Reynolds number is increased. Flow structures over these bodies change as the Reynolds number increases (Re). At Reynolds numbers below unity, the flow is fully attached with no separation. As Re is increased, the flow separates and a pair of steady symmetric vortices forms behind the body (Re $\approx$ 3.2-5 [1]). At higher Reynolds numbers, the vortex length of the re-circulation region behind the body grows as the Reynolds number increases. At a critical onset Reynolds number, Re_{cr1}, the twin-vortex arrangement becomes unstable, and a periodic oscillation wake and a staggered vortex street are

formed. The separated vortices are "shed" alternately from the upper and lower side of the body. The periodic phenomenon is referred to as vortex shedding, whereas the anti-symmetric wake flow pattern is referred to as the Von Karman vortex street. This is the first 2D wake transition called Benard-von Karman instability. This transition contains a 2D instability from a steady wake to a periodic wake. The physically relevant processes, which are associated with the vortex shedding, are the convection and dissipation of vorticity. If the dissipative mechanism dominates, vorticity dissipates before a wake instability can be excited, and thus a steady flow results. Conversely, when the convective forces dominate, the unsteady vortex shedding forms. The Reynolds number, which represents the ratio of convective to dissipative forces, is therefore physically relevant and serves as the bifurcation parameter. The earliest recorded observation of the phenomenon of the vortex shedding was reported by Leonnardo da Vinci in the sixteenth century when he sketched a double row of vortices in the wake of a bluff body. The near-wake flow unsteadiness gives rise to fluctuating drag and lift forces, which can stress the body by making it vibrate. By increasing the Reynolds number, a 3D transition is developed at around Reynolds number 200 (Re_{cr2}), and the three-dimensional flow effects appear [2, 3]. Within the laminar regime, which is between these two instabilities, ($Re_{cr1} < Re < Re_{cr2}$), the vortex shedding is characterized by a very well-defined frequency, which, when scaled with the viscous time scale, d^2/ν, exhibits an approximate linear increase with the Reynolds number [4]. As Re increases higher still, the effects of flow three dimensionality and turbulence become more and more pronounced.

The study of flow around a circular cylinder has been the subject of intensive investigations in recent years. The most recent works have investigated high Reynolds numbers, but there are comparatively few investigations, especially for heated bodies at low Reynolds numbers. Recently, a number of numerical investigations have been carried out to study the characteristics of heat transfer and fluid flow over cylinders at low Reynolds numbers [5-8].

The main objective of the present study is to provide reliable results from simulations of the flow around a heated circular cylinder for different Reynolds numbers ranging from 20 to 200 and to make comparisons with other available numerical and experimental results. Also, particular emphasis is put on the study of the first wake bifurcation (onset of vortex shedding), heat transfer and fluid flow near the wake.

2. ONSET OF VORTEX SHEDDING (HOPF BIFURCATION)

The development of a periodic flow emanating from a steady flow, causing periodic vortex shedding, is a Hopf bifurcation that can be modelled by the Stuart-Landau equation [9-11]. The onset of Karman vortex shedding is studied in the wake of different two-dimensional bluff bodies, experimentally [9-13] and numerically [4, 14, 15]. Provansal *et al.* [9] found that the periodic vortex street near the wake is the saturated end product of temporal global wake instability, and not a spatial response to continuously supplied upstream disturbances. It was also found that, for Reynolds numbers not too far above the critical one, the shedding frequency in the final saturation is not significantly different from the linear global response frequency, suggesting that an approach to vortex shedding from the linear stability theory has validity. They also showed that the wake dynamics could be described by a single Stuart-Landau (SL) equation by measuring all coefficients of the SL-equation for a range of Reynolds numbers near the onset of Karman shedding. It is important to mention that a non-stationary perturbation $u_1(x,y,z,t)$ of the steady solution $u_0(x,y,z)$ of the Navier-Stokes equations is expanded in order to perform the stability analysis of a steady flow as a sum: $u_1(x,y,z,t) = \sum_{i=1} \{A_i(t)g_i(x,y,z) + A_i^*(t)g_i(x,y,z)\}$, where $g_i(x,y,z)$ satisfies the boundary conditions [9-11,14]. It is shown that the amplitude $A_i(t)$ satisfies the evolution

equation $dA_i / dt = s_i A_i + G_i(A_j)$, where G_i contains the nonlinear interaction of all the modes resulting from the nonlinear partial differential equation [9]. A truncated form of this equation is named the landau equation (Eq. (1)), and can be employed to model the onset from steady to periodic flow (a Hopf bifurcation).

$$\frac{dA}{dt} = \sigma(p)A - \lambda M^2 A + O(M^5), \quad M = |A|, \quad A = M \exp(i\Phi t) \tag{1}$$

Where $A(t)$ is a characteristic complex amplitude associated with the fundamental frequency component, and $\sigma = \sigma_r + i\sigma_i$ and $\lambda = \lambda_r + i\lambda_i$ are both complex constants. In this equation, p represents a bifurcation parameter such as the Reynolds number. The physical meaning of σ_r, σ_i is that of the amplification rate and the angular frequency, respectively, of oscillations having infinitesimal amplitudes. These constants are global characteristics, which means that they are the same at all points of flow [16].

An amplitude equation and a phase equation (the real and the imaginary parts of Eq. (1)) are as:

$$\frac{dM}{dt} = \sigma_r M - \lambda_r M^3 \tag{2.1}$$

$$\frac{d\Phi}{dt} = \sigma_i - \lambda_i M^2 \tag{2.2}$$

This model has applicability if the onset of vortex shedding at the critical Reynolds number behaves as a Hopf bifurcation. In a linear regime, the second term on the right-hand side of Eq. (2.1) is negligible, and the disturbances will grow in the usual exponential manner at a rate that depends on the magnitude of σ_r. As the amplitude increases, nonlinear effects become more important, and the amplitude saturates to a certain level. The saturation state (denoted by suffix "*sat*") is given by the condition $dM/dt = 0$ in Eq. (2.1), or

$$M_{sat} = (\sigma_r / \lambda_r)^{0.5} \tag{3}$$

Following Landau and Stuart [17, 18], σ_r and σ_i are expanded in terms of the bifurcation parameter (Reynolds number) in a certain nontrivial neighbourhood of critical Reynolds number as:

$$\sigma_r(\mathrm{Re}) = \frac{d\sigma_r}{d\,\mathrm{Re}}(\mathrm{Re} - \mathrm{Re}_{cr}) + O(|\mathrm{Re} - \mathrm{Re}_{cr}|^2) \tag{4.1}$$

$$\sigma_i(\mathrm{Re}) = \sigma_i(\mathrm{Re}_{cr}) + \frac{d\sigma_i}{d\,\mathrm{Re}}(\mathrm{Re} - \mathrm{Re}_{cr}) + O(|\mathrm{Re} - \mathrm{Re}_{cr}|^2) \tag{4.2}$$

where Re_{cr} is defined by $\sigma_r(\mathrm{Re}_{cr}) = 0$. Equation (4) shows that growth (or decay) rates are a linear function of Reynolds number in the vicinity of critical Reynolds number. An expression for saturation or limit-cycle amplitude is obtained using Eq. (3) and 4 as:

$$M_{sat} = [\frac{1}{\lambda_r} \frac{d\sigma_r}{d\,\mathrm{Re}}(\mathrm{Re} - \mathrm{Re}_{cr})]^{0.5} \tag{5}$$

Combining Eqs. (2) and (4) and noting that $d\Phi/dt = 2\pi f$ where f is the frequency of oscillations in the disturbed state, it may be written as:

$$S = \frac{1}{M} \frac{dM}{dt} = \sigma_r - \lambda_r M^2 = \sigma_r(1 - R^2), \qquad R = M / M_{sat} \tag{6.1}$$

$$\frac{d\Phi}{dt} = 2\pi f = \sigma_i - \lambda_i M^2 = \sigma_i - (\sigma_r \lambda_i / \lambda_r)R^2 \tag{6.2}$$

The above relations show that the instantaneous growth rate, *S*, and instantaneous frequency, $\frac{d\Phi}{dt}$, are linear functions of the instantaneous amplitude (*M(t)*) squared. Equation (4) also can be used to obtain the coefficients of σ and λ.

Strictly speaking, Eq. (6) is valid only at Re very close to the onset. Based on experimental observation [10], they seem to be applicable for $(\mathrm{Re} - \mathrm{Re}_{cr})$ ranging from –10 to 25, approximately. From transient real measurements or numerical simulations at Reynolds numbers close to the onset, giving out different values of σ_r, the onset value of Re is determined by interpolation with equation 4. In the present study, the function *M* is, as in[14], chosen to be the lift coefficient. In this respect, as mentioned [4], the analysis relies on the fact that the linear growth rate is independent of location, i.e. vortex shedding results from a time-amplified global instability [9]. As also mentioned in [10], the vortex shedding during a start-up is always two dimensional. Thus, a two dimensional method for the prediction of the onset of vortex shedding is suitable.

3. NUMERICAL DETAILS AND PROBLEM DESCRIPTION

A fixed two-dimensional heated circular cylinder with diameter d is exposed to a constant free stream velocity U. All geometrical lengths are scaled with *d*. The scaling with *d* also applies to the Strouhal number, St=f d/U (*f* is the shedding frequency), forces and Nusselt number. Velocities are scaled with a constant free stream velocity, U, and physical times with d/U. The origin of force coordinates is placed at geometrical centre with drag force D positive in the x-direction and lift L positive in the y-direction. The non-dimensional temperature, T^*, is defined as $T^* = (T - T_O)/(T_W - T_O)$, where T_W is the constant temperature on the cylinder wall and T_O is the constant inflow temperature. The Nusselt number on the cylinder wall is computed as: $Nu = \frac{hd}{k} = -\frac{\partial T^*}{\partial n}$, where *h* is a convection coefficient. The time-dependent calculation is started with the fluid at rest and a constant time step Δt =0.02 is used for all simulations. A non-uniform O-type grid is used. Some studies on the effect of grid distribution, grid size and the number of grid points are performed using resolutions up to 90000 grid points. Based on these results and also refinement studies of previous works of the present author [4, 19], it seems that a resolution of 40000 grid points with a solid blockage of about 3% is sufficient to obtain accurate results where discrepancy between the global results of the finest grid and this resolution is less than 5 percent. A uniform flow ($u_1 = U$, $u_2 = T^* = 0$) is prescribed at the inlet as boundary condition. At the outlet, the convective boundary condition [4] is used for all velocity components and temperature. A No-slip condition is prescribed on the body. T^* is set to one on the cylinder wall, where $T = T_W$.

The flow is assumed to be two-dimensional and unsteady. An incompressible SIMPLEC finite volume code is used employing a non-staggered grid arrangement. The scheme is implicit in time, and a Crank-Nicolson scheme, which is of second order, has been used for convective and diffusive terms and the pressure is treated fully implicitly. The convective terms are discretized using the QUICK differencing scheme, whereas the diffusive terms are discretized using central differences. More details of the code, equations etc. are described in [19]. The governing equations of this work in dimensionless form are as follow:

$$\frac{\partial u_i}{\partial x_i} = 0 \tag{7}$$

$$\frac{\partial u_i}{\partial \tau} + \frac{\partial (u_i u_j)}{\partial x_j} = -\frac{\partial p}{\partial x_i} + \frac{1}{\mathrm{Re}} \frac{\partial^2 u_i}{\partial x_j \partial x_j} \tag{8}$$

$$\frac{\partial T^*}{\partial \tau} + \frac{\partial (u_i T^*)}{\partial x_i} = \frac{1}{\text{Re Pr}} \frac{\partial^2 T^*}{\partial x_i \partial x_i} \tag{9}$$

In deriving these equations, the following assumptions are made. The flow is assumed incompressible with constant fluid properties Also the natural convection and viscous dissipation effects are neglected. Lange *et al*. [5] presented some results and showed the validity of these assumptions for Re<200.

4. RESULTS AND DISCUSSION

Simulations of 2D-unsteady flow around a heated circular cylinder for low Reynolds numbers ($ \text{Re} = 20 - 200 $) are performed. The onset of vortex shedding is studied using the Stuart-Landau Equation. The structure of the flow is studied close to the oscillation threshold and also at the higher Reynolds numbers using streamlines, pressure, vorticity and the second invariant of velocity gradient tensor contours. Some useful physical quantities such as Nusselt numbers, the dominating wake frequency (Strouhal and Roshko numbers), mean drag and the RMS value of lift are computed and compared with numerical and experimental results.

a) Onset of vortex shedding

A study on the onset of vortex shedding is carried out using the Stuart-Landau Equation as outlined in section 2. Based on this study, the Reynolds number and frequency of the actual onset are predicted. It is important to mention that the shedding frequency is normalized with both the convective time scale, (d/u), and the viscous time scale, (d^2/v). The shedding frequencies scaled in this way are usually referred to as Strouhal number ($St = fd/u$) and Roshko number ($Ro = fd^2/v = \text{Re} \times St$), respectively.

The time-dependent simulations are started with the fluid at rest. The transient periods, before the fully saturation state is achieved are different, ranging from about a 25000 time step for a low Reynolds number, close to the onset of vortex shedding, to about 2000 time step at Re=200 (Fig. 1). At low Reynolds numbers, the flow oscillations take a rather long time to develop if one is in very close positive vicinity of critical Reynolds number. From Fig. 1, the typical oscillation of lift fluctuations are seen for two cases; first, at subcritical state (e.g. Re=45) where the amplitude of the signal decays to a zero level, in which the wake flow becomes steady and there is no vortex shedding in the wake. The second supercritical state (case Re=80 in Fig. 1), where signal amplitude grows to a certain constant level, the fully saturation state and the vortex shedding process occur in the wake flow. Similar signals are also observed when the Reynolds number is less than a critical value (subcritical state) or greater than a critical value (supercritical state).

The following procedure is adopted for determining the critical Reynolds number and frequency, when the vortex shedding commences. As mentioned in Section 2, the lift coefficient is selected as the signal in this analysis (Eq. (1) and Fig. 1). For each Reynolds number close to the onset of vortex shedding, the value of growth, or decay rate (σ_r), is found from Eq. (6.1) by fitting a straight line in a plot of the non-dimensional instantaneous growth rate S versus R^2, instantaneous non-dimensional amplitude squared, as suggested by the SL-model (Eq. 6.1). The value of σ_r is equal to S value at a location where this fitting line to data crosses the S axis (where R=0), (Eq. (6.1) and Fig. 2 (left)). By this method, the values of σ_r are obtained for different Reynolds numbers ranging from 45 to 200. The same procedure is also used to find the critical frequency and the other constant in the SL-equation, (Eq. (1)). To determine the constants of Eq. 6b, the instantaneous Roshko numbers are plotted versus instantaneous amplitudes squared as suggested by the SL-model. By fitting a line in the data and extrapolating the line to zero amplitude, the starting frequency or starting Roshko number ($Ro_0 = \sigma_i d^2 / 2\pi v$) was found at each

A. Sohankar

Reynolds number. The saturation Roshko number was also determined at the location where the amplitude reaches to constant level, (Figs. 1 and 2).
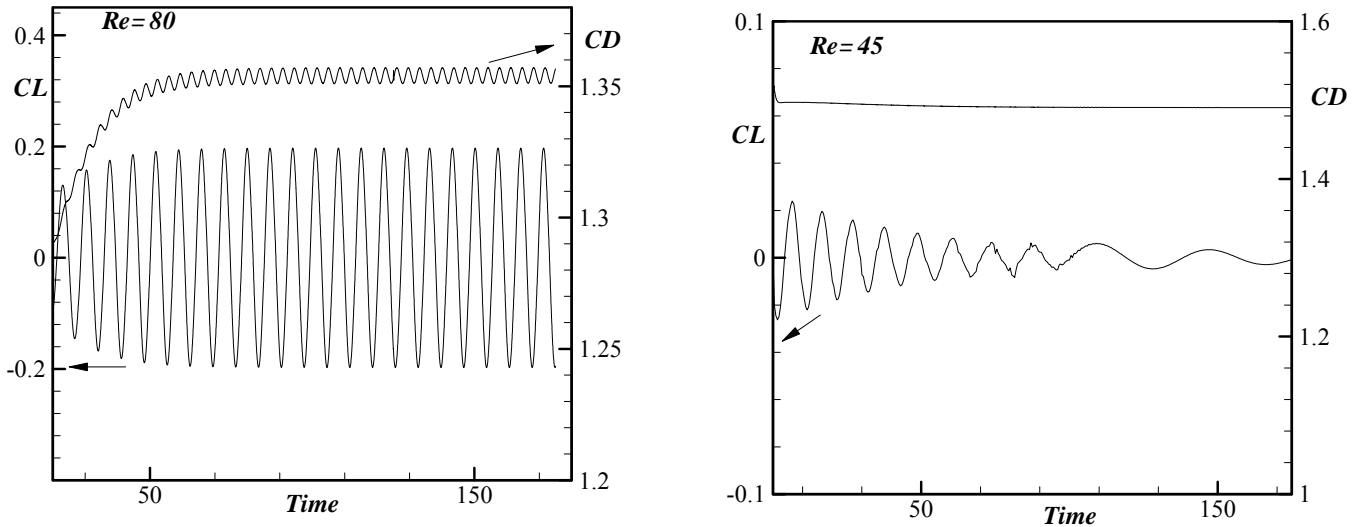

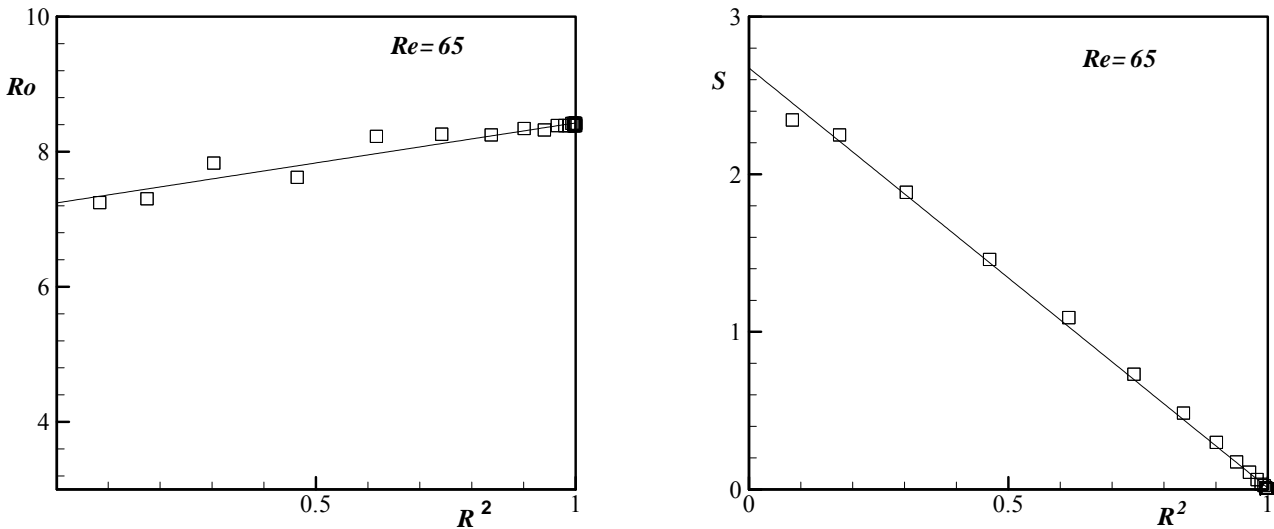Fig. 1. Time evolution of lift and drag coefficients (M=CL), with (Re=80) and without (Re=45) vortex shedding

Fig.2. Instantaneous growth rate (left) and instantaneous Roshko number(right) versus normalized-amplitude squared during amplification at Re=65

By using data similar to Figs. 1 and 2, the values of σ_r, Ro and Ro_0 (or σ_i) at various Reynolds numbers are obtained. The results for σ_r and Ro are collected for different Reynolds numbers in Fig. 3. In Figs. 2 and 3, the σ_r and σ_i are normalized with the viscous time scale. Based on Eq. 4, the value of Re_{cr} is determined by condition $\sigma_r(Re_{cr}) = 0$. Thus, by fitting a line to data in Fig. 3 (left) and finding the corresponding value of Re, where σ_r is equal to zero, the critical Reynolds number is determined to be Re_{cr}=49. The critical frequency of flow (in non-dimensional form is St_{cr} or Ro_{cr}) is determined from Fig. 3 (right) at Re_{cr}, which is $St_{cr} = 0.12$ and Ro_{cr}=5.85. By using the results displayed on Figs. 2 and 3, and using the relations in section 2, the following results are obtained:

$$Ro = 5.85 + 0.207(\text{Re} - \text{Re}_{cr}) \qquad \text{or} \qquad St = 0.207 - 4.3/\text{Re}$$

$$\sigma_r = 0.156(\text{Re} - \text{Re}_{cr}) \qquad \text{where} \quad d\sigma_r/d\text{Re} = 0.156$$

$$\sigma_i = 32.38 + 0.68(\text{Re} - \text{Re}_{cr}) \qquad \text{where} \quad d\sigma_i/d\text{Re} = 0.68, \ \sigma_i(\text{Re}_{cr}) = 32.38$$

Table 1 compares the critical Reynolds number, Strouhal number and Roshko number of this study with experimental [9, 10, 12, 13] and numerical [15] ones. The critical values of this study for the onset of periodicity are in good agreement with experimental and numerical ones, although the discrepancy with a numerical one is larger. It seems that this discrepancy is mostly due to using a relatively coarse grid and high blockage (about 10%) [15]. It is important to mention that the SL-model is valid at Re close to the onset, where the difference between Re and critical Re at the onset is not larger than about 25 [10]. As seen from Fig. 3 (left), when only the data between Re=45 and Re=75 is used, the critical Reynolds number is Re_{cr}=49, while this value is Re_{cr}=46.7 when data is chosen between Re=45 and Re=150 (this figure is not shown here). This result is also in good agreement with the experimental ones. The corresponding values for the critical Strouhal number for these two cases are 0.120 and 0.115, respectively. It is believed that the Re_{cr}=49 and the corresponding values for St_{cr} and Ro_{cr} are more realistic than 46.7, because the conceptual basis of the SL-model is built on a Hope bifurcation which is purely temporal in nature. At *Re* far from the onset of vortex shedding *(Re>150),* the wake flow become 3D [2, 3] and spanwise effects can change the structure of the wake flow, thus using a temporal model is questionable. The wake flow at higher Reynolds number (Re>200) is well modelled with the Ginzburg-Landau model [20] where Re and aspect ratio are wake parameters.
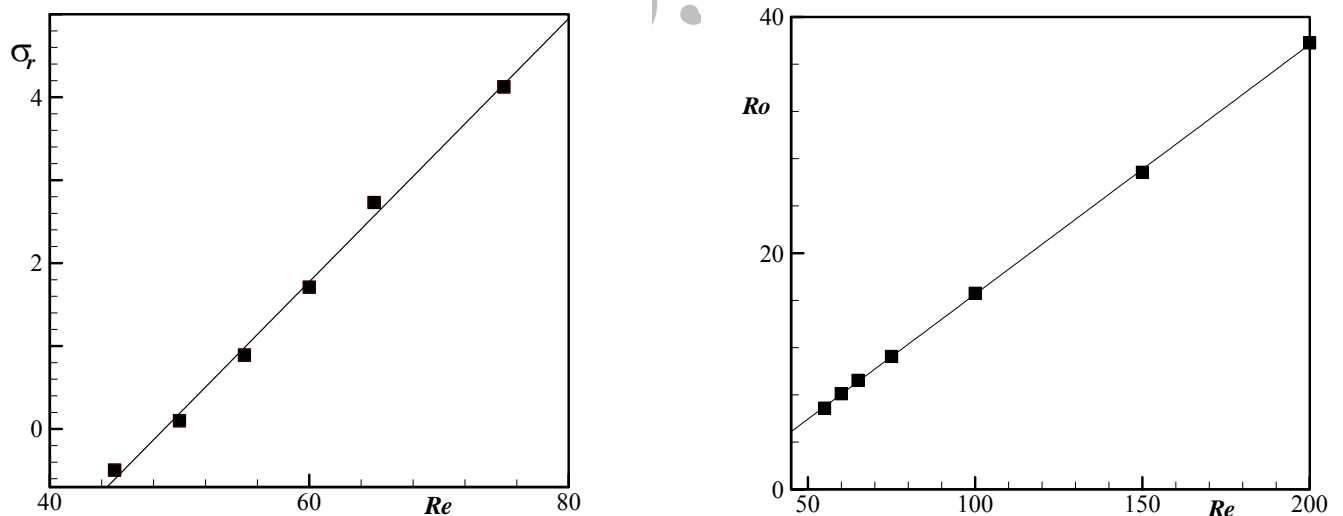

Fig. 3. Linear global growth rate (left) and Roshko number (right) versus Reynolds numbers

Table 1. Comparison of the results of this study with experimental and numerical ones

	Exp.[9]	Exp.[10]	Exp.[12]	Exp.[13]	Num.[15]	This study
Re_{cr}	47	47	48	47.4	46.2	49, 46.7
St_{cr}	-------	0.115	0.12	0.116	0.138	0.12, 0.115
Ro_{cr}	--------	5.41	5.76	5.5	6.38	5.85, 5.37

b) *Wake flow structure*

In this section, some aspects of wake flow features are studied using instantaneous vorticity, pressure and the second invariant of velocity gradient tensor, $Q = 0.5(u_{i,i}u_{j,j} - u_{i,j}u_{j,i})$, contours and streamlines (Figs. 4 and 5). To study instantaneous-flow structure, it is necessary to recognize the significant vortical regions in the flow field. It is important to mention that a vortex should have a vortex core with a net vorticity and the geometrical characteristics of the identified vortex must be Galilean invariant [21]. Because an agreement on the definition of a vortex does not yet exist, it is difficult to recognize the general vortical structure for all flow cases, especially in 3D flow, with only one method, where these requirements for the vortex core may not yield a single scheme. Therefore, several methods such as using streamlines, pathlines, vorticity, pressure, the rate of strain tensor, etc are propounded for identification and visualization of vortical structures [21]. In the present work, the instantaneous flow structures were studied using vorticity, streamlines, pressure and the second invariant of the velocity gradient tensor. It is worth mentioning that a region with a pressure value lower than the ambient one and a positive second invariant of velocity gradient tensor ($Q = 0.5(u_{i,i}u_{j,j} - u_{i,j}u_{j,i}) > 0$) is also defined as a vortex core [22].
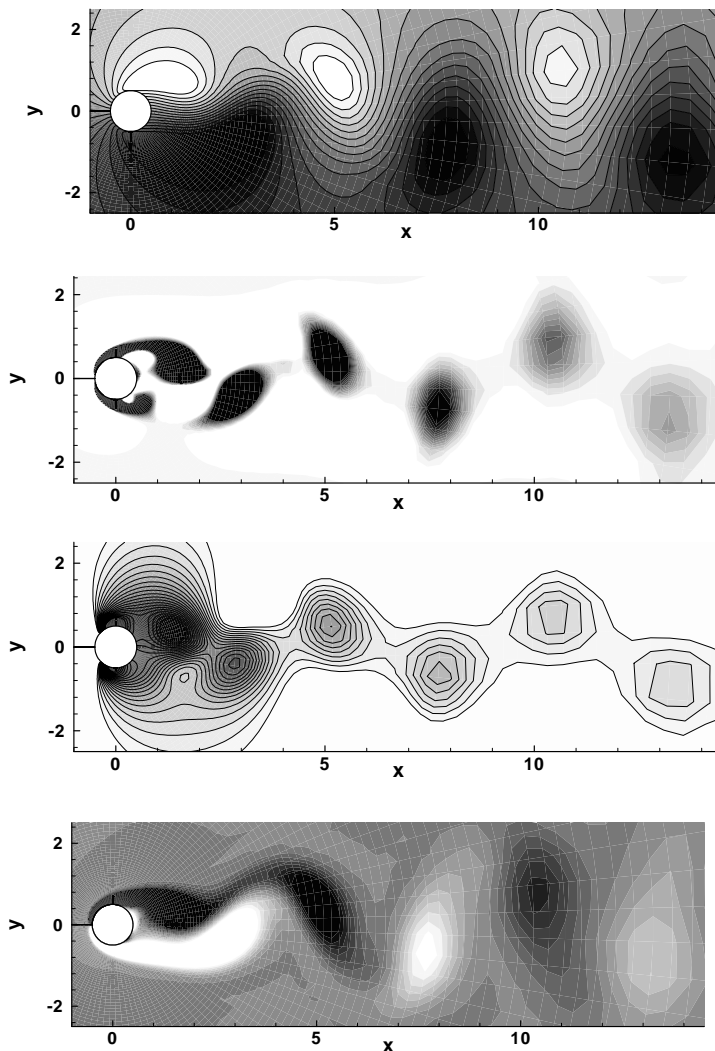

Fig. 4. From top to bottom, streamlines, the positive second invariant of velocity gradient tensor
($Q = 0.5(u_{i,i}u_{j,j} - u_{i,j}u_{j,i}) > 0$), pressure and vorticity contours
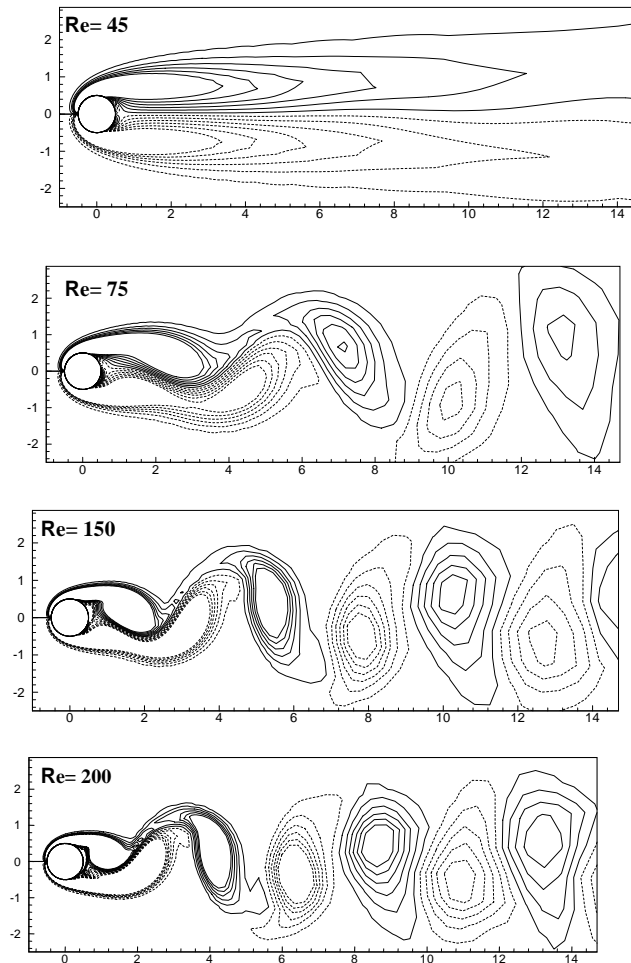at one time instant, Re=100

Fig. 5. Instantaneous vorticity contours for different Reynolds numbers, solid lines
(clockwise, negative) and dashed lines (anti-clockwise, positive)

The instantaneous vortex street formation at one instant was provided with the aforementioned methods for Re=100 in Fig. 4. As seen, the structure of vortex cores in the wake region behind the body is clearly predicted with these four methods, while the vorticity and especially Q contours, clearly identify the vortical structure in a better way. From plots in Fig. 5, the vortex street formation is seen for different Reynolds numbers. At supercritical state $(\text{Re} > \text{Re}_{cr})$, these vorticity contours are chosen at a time instance during the fully saturated state where the maximum amplitude remains constant with time (Fig. 1(right) for $t > 50$ at Re=80). At sub-critical state ($\text{Re} < \text{Re}_{cr}$), where the amplitude of force signals decays to zero level, the flow approaches to steady and there is no vortex shedding. It is observed from Fig. 1 at $t > 100$ (Re=45) that the level of lift coefficient is about zero. The corresponding vorticity contour for one time instant in this region is depicted in Fig. 5. As seen, the flow is symmetric and two attached vortices are observed with no vortex shedding. Similar behaviour is also seen for the other instances and also all other cases with $\text{Re} < \text{Re}_{cr}$. This verifies the previous finding in section 4a, where the onset of vortex shedding was predicted at $\text{Re} = 49$.

By increasing the Reynolds number from the onset value ($\text{Re}_{cr} = 49$), the flow around the body exhibits an oscillatory behaviour, instantaneous flow becomes asymmetric with respect to the oncoming flow, the twin-vortex arrangement becomes unstable and a time-periodic oscillation of the wake develops, which is called vortex shedding. This phenomenon is clearly seen in Fig. 5 for Re=75,150,200. The solid and dashed lines in theses plots correspond to vortices, which shed from the upper and lower side of the body in a clockwise and anti-clockwise direction, respectively.

The process of vortex shedding is periodic, meaning that the formation and the shedding of vortices are repeated during a time period. Thus, the same plots with Fig. 5 were also observed after a time period. This time period becomes shorter with the increase of the Reynolds number. A shorter time period causes the shedding frequency (or Strouhal number in non-dimensional form) to increase. The higher frequency means that the process of vortex shedding is faster. During a time period, two vortices form and shed; one from the upper side and another from the lower side. At low Reynolds number, e.g. Re=75, the free shear layers from the upper side (or lower side in the other half period) are extended farther downstream in comparison to the cases with higher Reynolds numbers, before rolling up to spanwise vortices. Thus, in the high Re cases, the first vortex shed in the wake at a position closer to the body (or in a shorter time). For example, these positions are located in a wake region with x=9, 6, 4, 3, approximately, for Re=55, 75, 150, 200, respectively (Fig. 5).

By increasing the Reynolds number from the onset value, the vortices become stronger. For example, the absolute values of the peak vorticity for the first shedding vortices in the vortex street are about 0.71, 1.02, 1.9, 2.61 for Re=55, 75, 150, 200, respectively. Stronger vortices cause higher (negative) pressure in the wake and also base pressure. This causes a higher pressure drag force to be obtained.

The magnitude of the peak vorticity associated with vortices decreases in the streamwise direction for each Reynolds number. As an example, for Re=200, the sequence of absolute peak values in the streamwise direction are 2.61, 1.84, 0.95, 0.76, respectively. At the centre of each vortex, there is a minimum pressure. These minimum values increase in the streamwise direction. Thus, it was observed that an increase in the pressure at the centre of each vortex correspond to a decrease in the magnitude of the peak vorticity in the streamwise direction downstream of the body.

To study the near wake and flow separation and attachment from the sides of the body, a number of instantaneous streamlines, isothermal lines, corresponding values of pressure coefficient, Cp, wall vorticity ω, and local Nusselt number, Nu, around the body at different time instances and Reynolds numbers were provided (Figs. 6-8 for Re=130). Attachment and separation points along the body were determined at some time instances and were labelled in the plots of Figs. 6 and 8 with a and s, respectively. It is important to mention that the θ is measured in a clockwise direction from the stagnation point. Thus the upper and the lower parts of the body correspond to $\theta \leq 180^{\circ}$ and $180^{\circ} \leq \theta \leq 360^{\circ}$, respectively. Due to periodicity of the flow in the fully developed state, where the force signal amplitude reaches constant levels, only some instants during one shedding period were considered.

Contrary to flow around rectangular cylinders, where the sharp corners are natural points of separation [4, 19], the separation points vary with time and oscillate forward and backward on the cylinder wall (Figs. 6, 8 and 11(right)). In Fig. 8, the variation of the wall vorticity is also observed, where the separation, stagnation and attachment points correspond to points of zero wall vorticity. In each time instance in these figures, the wall vorticity is positive below zero and negative above zero at the separation points (labelled with s), while the wall vorticity is negative below zero and positive above zero at the attachment points (labelled with a).

Instantaneous streamlines and the corresponding values of the pressure coefficient, Cp, and wall vorticity, ω, around the body in four time instances during approximately a half period of vortex shedding for Re=130 were shown in Figs. 6-8 The first plot in these figures was chosen at t=104, where the lift coefficient has a negative value (CL=-0.362) and it is close to a minimum lift (CL_{min}=-0.378 at t=104.3). It is seen that an anti-clockwise vortex is in development due to separation at the lower part of the body. As it grows, with increasing strength but being rather fixed in position, the attachment point on the rear side is being pushed upward. As the attachment point reaches more or less to a point on the upper side, the lift already has passed its minimum level (CL=-0.378 at t=104.3) and a new clockwise vortex is about to be formed at the upper part of the body (second plot at t=104.75 (CL=-0.338)). As this new vortex grows, the old clockwise vortex is being pushed away and is eventually shed into the wake, (plots at t=104.75 and

t=105.5 in Figs. 6). As seen from these plots, an anti-clockwise vortex forms and is shed during this half period. During the next half period, the new clockwise vortex (see plot at t=107 where the lift force is close to maximum lift value) grows and sheds with a similar trend as explained for the old vortex (due to lack of space these plots were not shown here). In general, the same trend was also observed for the other Reynolds numbers of this study above the onset of vortex shedding, but with different variations in the locations of separation and attachment points, lift, drag, Nusselt number and so on.
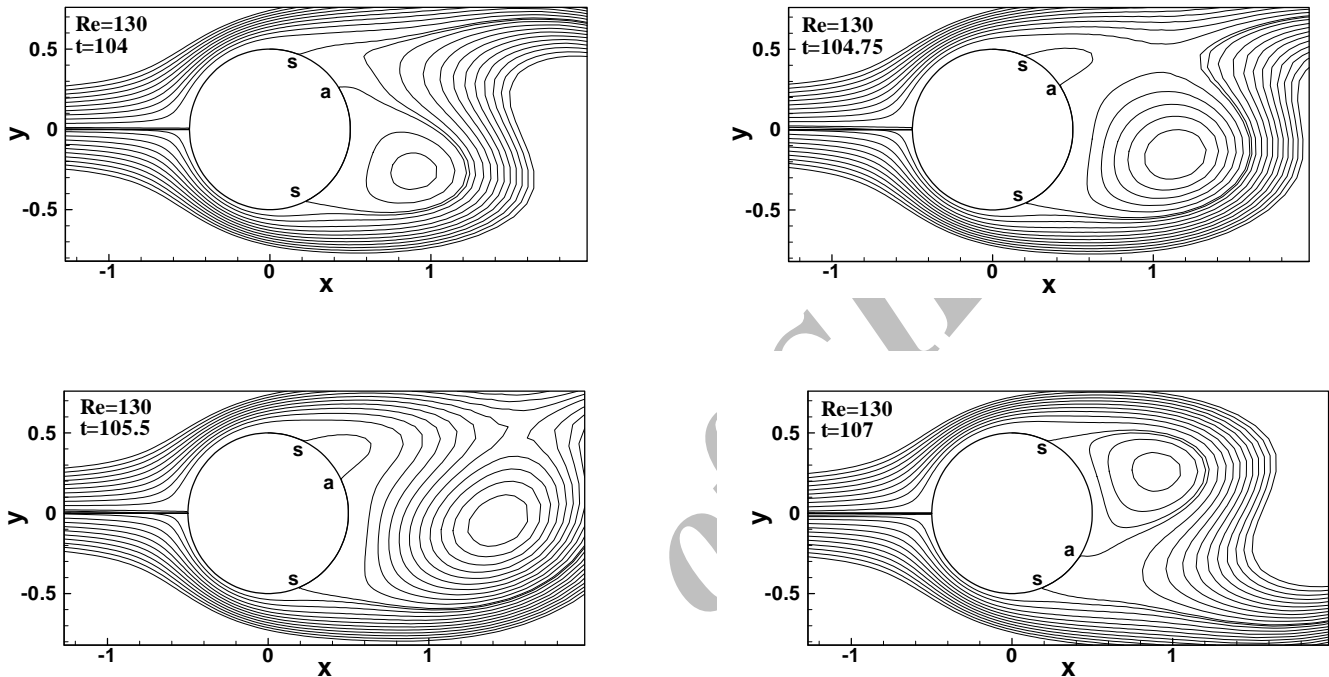
Fig. 6. Instantaneous streamlines at four chosen instants during
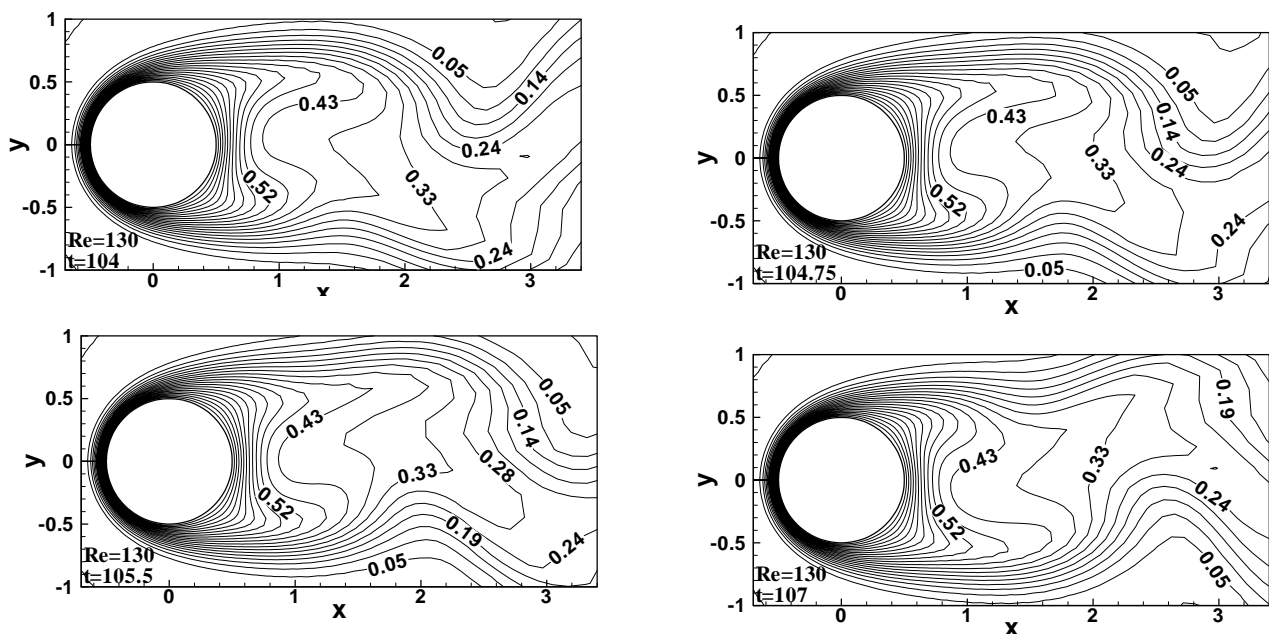one cycle of vortex shedding process

Fig. 7. Instantaneous normalized temperature (T^*) isolines at four chosen
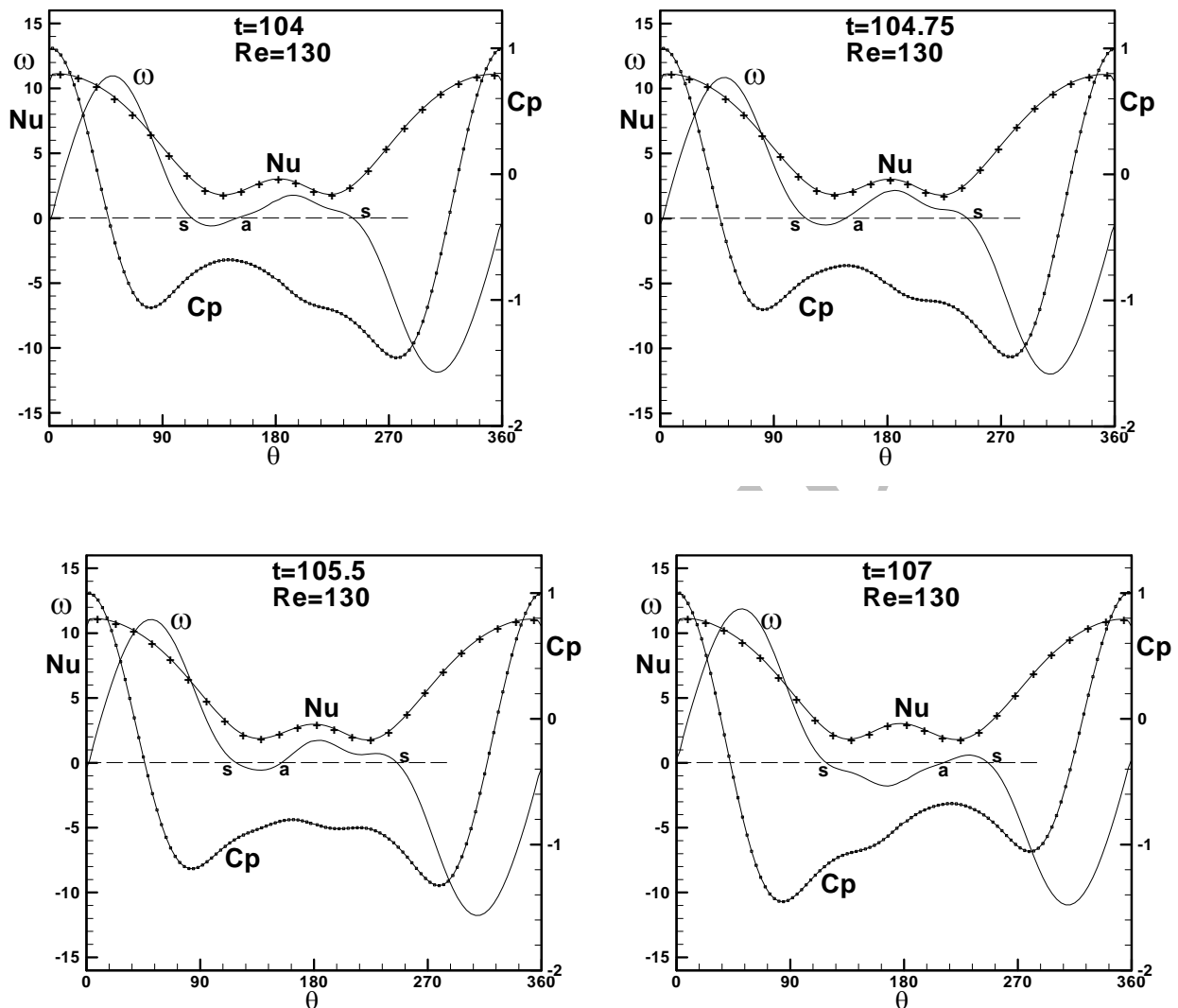instants during one cycle of shedding process

Fig. 8. Instantaneous Nusselt number (*Nu*), pressure coefficient (*Cp*) and wall vorticity *(ω)* around
the body at four chosen instants during one cycle of vortex shedding process

The locations of separation on the upper, θ_{s1}, and the lower, θ_{s2}, parts of the body and also the attachment (θ_a) move along the body surface with time (Figs. 6, 8 and 11(right)). The variation ranges of θ_s with time for a low Reynolds number is not much, but it increases as the Reynolds number increases. For example, these are about $\theta_{s1} \cong 123$-124, $\theta_{s1} \cong 119$-122.7 and $\theta_{s1} \cong 111.5$-119.8 on the upper part of the body for Re=55, 80, 160, respectively.

Instantaneous non-dimensional temperature, T^*, and isolines for different Reynolds numbers from 20 to 200 are provided in this study (Fig. 7 for Re=130). In this figure, the isotherms were plotted with an interval of 0.0475 from zero to one. As mentioned above, the flow became unsteady due to the loss of stability of the symmetric wake and the vortices shed from the rear part of the body. The results of this study show that the upper and lower symmetry of isolines in the wake regions for Re<49 are progressively destroyed as the Reynolds number is increased. This asymmetry in pressure and wall vorticity is higher than the temperature and Nusselt number (Fig. 8).

By increasing the Reynolds number, the higher asymmetry and more complicated patterns appear in the wake region behind the body, whereas no asymmetry is seen in the frontal part of the body. Much sharper temperature gradients (or higher local Nusselt numbers on the wall) occur closer to the body as the Reynolds number increases. This effect is higher in the frontal part than in the rear part of the cylinder and

causes higher local Nusselt numbers to be produced at the front part of the body. This is clearly observed from Fig. 7, where the isothermal lines are shown for four instances during a half cycle of vortex shedding at Re=130. The variation of local Nusselt numbers over the body at four time instances for Re=130 are shown in Fig. 8. Based on this figure and also the study of local Nusselt numbers for other Reynolds numbers of the present study, it is observed that the local Nusselt number distribution around the body is affected by the boundary development on the front part of the cylinder and by separation and wake instability over the rear part of the body. The maximum local Nusselt number occurs at stagnation point, where the boundary layer is thinnest and hence resistance to heat transfer is at a minimum. It is important to mention that the position of the stagnation point in unsteady cases has a small variation at around $\theta=0$. The minimum local instantaneous Nusselt number on the body depends on the Reynolds number and is located at a point between the separation and attachment points, Fig. 8. The mean time locations of the minimum Nusselt number also depend on the Reynolds number. For example, these points occur at angles of 142, 138, 136 and 132 approximately, for Reynolds numbers of 80, 130, 160 and 200, respectively.

c) Global quantities

The global results at various Reynolds numbers up to 200 are provided for a blockage of 3% in Figs. 9-11. These computed global quantities dominate wake frequency (Strouhal number, *St*), mean Drag coefficient (CD), RMS value of lift (CL'), mean separation angles (θ_S) and mean Nusselt number ($\overline{Nu}$). For Reynolds number less than 50, the flow is steady and lift and RMS values of lift and drag are zero. At $Re \geq 49$, the effects of instabilities appear, which cause vortex shedding, and the wake flow becomes unsteady, (Fig. 1 for Re=80). The global quantities are calculated from unsteady Nusselt number, lift, drag, separation and attachment signals during the fully developed vortex shedding phase, where the maximum and minimum of these quantities reach constant levels (Fig. 1(right) for $t > 50$). For all cases, the fully developed state could be described with a signal well-defined shedding frequency. The transient period, before the fully developed state is achieved, depends on Reynolds numbers ranging from about a 600 time unit for Re=50 to a 50 time unit at Re=200 (Fig. 1(left)).

As seen from Fig. 9, with increasing the Reynolds number the Strouhal number increases continuously and shows a good agreement with the experimental results [2, 13] up to $Re = 150$. As mentioned in section 1, a 3D transition is developed around a Reynolds number of 200 and the three-dimensional flow effects appear. As noted by Williamson [2], this transition is associated with an hysteric discontinuity in the Strouhal number values. Due to this phenomena, there is a reduction in the Strouhal number at around the transition Reynolds number and then increasing up to $Re \approx 300$ [2]. This can interpret the difference between a 2D computed Strouhal number and 3D experimental ones at $Re = 200$.

The variation of the averaged drag coefficient with Reynolds number is shown in Fig. 9. The drag coefficients obtained in this study are compared with the results of Park et al. [23] (Blockage: 1%, Grid: 641×241), Franke *et al.* [24] (Blockage: 2.5%, Grid: 140×144 grid), 2D and 3D simulations of Zhang and Dalton [25] and Rosenfeld[26] (Grid: 513×513) (Fig. 9(right)). As seen from this figure, the drag coefficient decreases continuously by increasing the Reynolds number up to 150. In this range of the Reynolds number, there is a good agreement with other results. Due to the appearance of three-dimensional flow effects for $Re > 150$, it is expected that the results from the 2D-simulations deviate from the 3D-results. This is clearly seen in Fig. 9 for $Re = 200$, where a discrepancy is observed between the 3D-data of Zhang & Dalton [25] and the present study, and also other investigations.

The RMS (root mean square) lift coefficients are calculated and shown in Fig. 10(right). As noted, the onset of vortex shedding is also the onset of fluctuating forces. Thus, the RMS values are zero for $Re < 50$. By increasing the Reynolds number from the onset value, the RMS values increase rapidly as the Reynolds number is increased. Norberg [27] reviews previous numerical and experimental investigations

concerning fluctuating lift acting on a circular cylinder and suggests a number of empirical functions for different quantities such as RMS lift, i.e. $CL' \approx (\delta/30 + \delta^2/90)^{0.5}$, $\delta = (Re - Re_{cr1})/Re_{cr1}$ for $47 \le Re \le 190$. Re_{cr1} is the critical Reynolds number, where the onset of vortex shedding occurs. It is selected as $Re_{cr1} \approx 47$ [27]. The results of this work are compared with Norberg's empirical function, (Fig. 10(right)) for two critical Reynolds numbers of 47 and 49. As seen, the agreement between the results is good, especially when a value of 49 is chosen for Re_{cr1} (denoted with asterisk in Fig. 10).
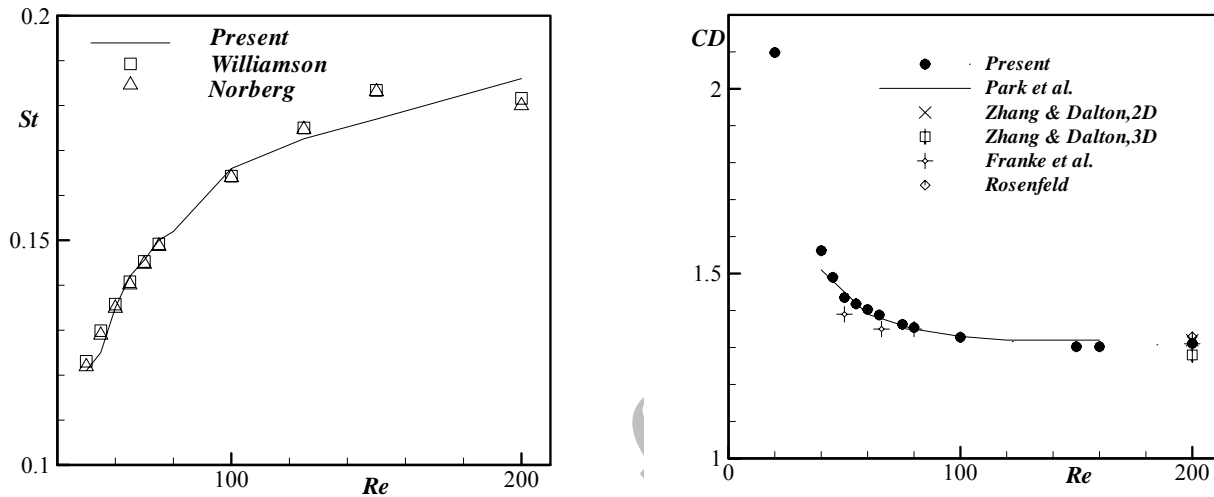

Fig. 9. Variation of Strouhal number (left) and drag coefficient
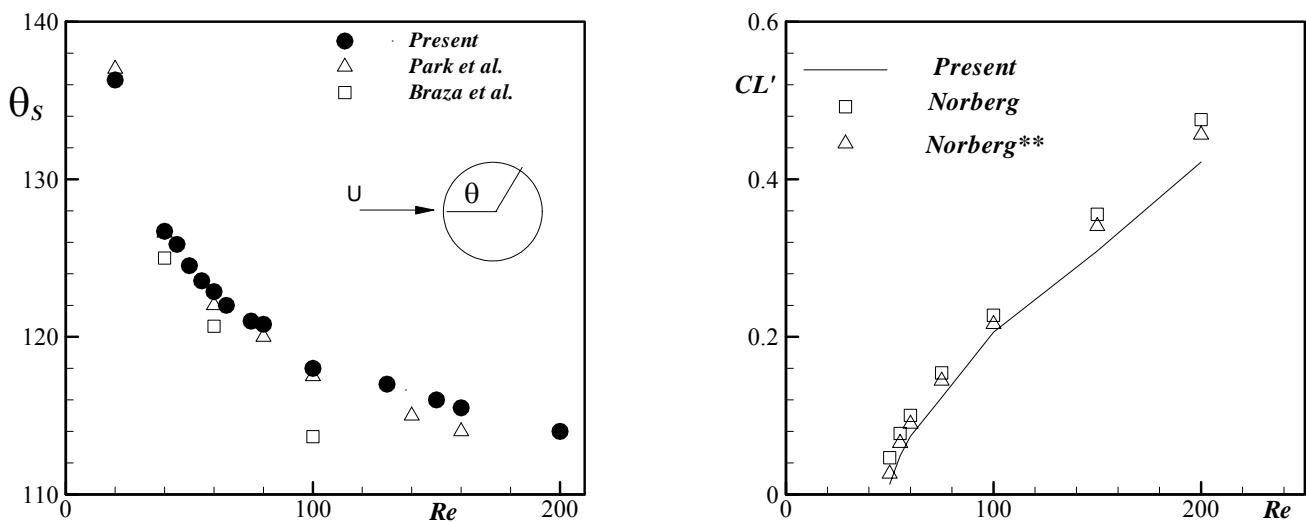(right) versus Reynolds number

Fig. 10. Variation of mean separation angle (left) and RMS lift
coefficient (right) versus Reynolds number

The variation of time mean separation angle on the upper part of the body with the Reynolds number is shown in Fig. 10 (left). The value of the mean separation angle decreases continuously (or wake size increases) as the Reynolds number increases. In this range of Reynolds numbers, there is a relatively good agreement with the results of Park *et al*. [23]. It is seen that the discrepancy between the present study and the results of Braza *et. al*.[28] is larger. It seems that this discrepancy is mostly due to using a relatively coarse grid and a high blockage (about 10%) by Braza *et. al*. [28]. By using the least-squares fitting, the

separation angles can be described by a single equation as $\theta_s = \exp\left[5.265(Ln(\text{Re}))^{-0.0637}\right]$. This equation represents the data of the present study with a maximum error smaller than one percent in the computed range of $20 \le \text{Re} \le 200$.

The averaged Nusselt number around the cylinder wall at each time instance (Nu, e.g. see Fig. 11right) and time-averaged Nusselt number ($\overline{Nu}$, see Fig. 11 left) per cycle are calculated as follows:

$$Nu = \frac{1}{2\pi}\int_0^{2\pi} Nu_\theta \, d\theta, \qquad \overline{Nu} = \frac{1}{\tau}\int_0^{\tau} Nu \, d\tau$$
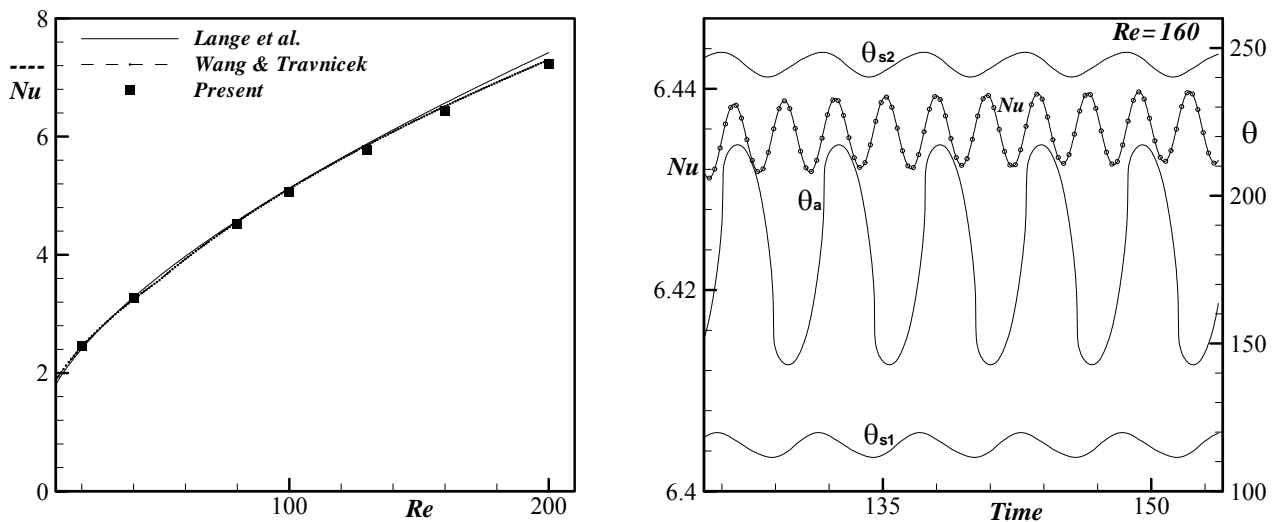

Fig. 11. Left: Variation of mean Nusselt number versus Reynolds number, Right: time history of Nusselt number, separation and attachment angles for Re=160

For example, the time variation of the Nusselt number for Re=160 is shown in Fig. 11(right). The level of fluctuations of Nu is not much if one compares it with time-averaged value. It increases by increasing the Reynolds number. For instance, the range of time variation of the Nusselt number during a period is Nu=6.435±0.005 for Re=160 (see Fig. 11(right)).

The variation of $\overline{Nu}$ with the Reynolds number is shown in Fig. 11(left) and they are compared with the experimental [7] and numerical [5] ones. It is seen from this figure that the $\overline{Nu}$ continuously increases as the Reynolds number is increased and there is excellent agreement between the present results and the experimental and numerical ones. It is important to mention that Lange *et al.* [5] and Wang and Travnicek [7] have included the temperature dependence of the Reynolds number on their results, due to the temperature variation between the fluid and the cylinder wall and their effects on the viscosity of fluid, by introducing an effective (or reference) temperature as: $T_{eff}/T_0 = 1 + C(Tw - T_0)/T_0$. The chosen values for C-coefficient were 1 (for $Tw/T_0 \le 1.5$) and 0.36 (for $Tw/T_0 \le 3$) by references [7] and [5], respectively. In spite of including this effect by [5,7], the constant property results of the present investigation have negligible discrepancy with those results. By using the least-squares fitting, the time mean Nusselt number versus Reynolds numbers can be described by a single equation as $\overline{Nu} = 0.165 + 0.495\,\text{Re}^{0.5}$. This equation represents the data of the present study with a maximum error smaller than one percent in the computed range of $20 \le \text{Re} \le 200$.

5. CONCLUSIONS

An unsteady solution of the incompressible Navier-Stokes equations is performed using a finite volume SIMPLEC code. The physical problem is flow over a heated circular cylinder for a Reynolds number

between 20 and 200. It is shown that the flow behind a circular cylinder is steady up to Re=49 and beyond this critical value, the flow develops to a periodic state, corresponding to the vortex shedding and force oscillation on the body. It is also shown that by increasing the Reynolds number from the onset value, the process of vortex shedding becomes stronger, which causes the mean Nusselt number, Strouhal number, lift and RMS lift coefficients to increase continuously by increasing the Reynolds numbers, whereas drag coefficient and mean separation angle decrease. Based on the results of this work, the empirical functions for Rosko, Strouhal and mean Nusselt numbers and also separation angle are suggested.

REFERENCES

1. Zdravkovich, M. (1997). *Flow around circular cylinders*. Oxford Science publication.

2. Williamson, C. H. K. (1996). Vortex dynamics in the cylinder wake. *Annu. Rev. Fluid Mech., 28*, 477-539.

3. Sohankar, A., Norberg, C. & Davidson, L. (1999). Simulation of unsteady 3D flow around a square cylinder at moderate Reynolds number. *Physics of Fluids, 11*, 288-306.

4. Sohankar, A., Norberg, C. & Davidson, L. (1998). Low-Reynolds number flow around a square cylinder at incidence: Study of blockage, onset of vortex shedding and outlet boundary condition. *I. J. for Numerical Methods in Fluids, 26*, 39-56.

5. Lange, C. F., Durst, F. & Breuer, M. (1998). Momentum and heat transfer from cylinders in laminar cross flow at $10^{-4} \leq \text{Re} \leq 200$. *I. J. of Heat and Mass Transfer, 41*, 3409-3430.

6. Lange, C. F., Durst, F. & Breuer, M. (1999). Wall effects on heat losses from hot-wires. *I. J. of Heat and Fluid flow, 20*, 34-47.

7. Wang, An-Bang & Travnicek, Z. (2001). On the linear heat transfer correlation of a heated circular cylinder in laminar cross flow using a new representative temperature concept. *I. J. of Heat and Mass Transfer, 44*, 4635-4647.

8. Fu, Wu-Shung, & Tong, Bao-Hong (2002). Numerical investigation of heat transfer from a heated oscillating cylinder in a cross flow, *I. J. of Heat and Mass Transfer, 45*, 3033-3043.

9. 9. Provansal, M., Mathis C. &. Boyer L. (1987). Benard-von Karman instability: transient and forced regimes. *J. Fluid Mech., 182*, 1-22.

10. Schumm, M., Berger, E. &. Monkewitz, A. (1994). Self-excited oscillations in the wakes of 2-D bluff bodies and their control. *J. Fluid Mech., 271*, 17-53.

11. Park, S. (1994). Theoretical analysis of feedback control of Karman vortex shedding at slightly supercritical Reynolds numbers. *Eur. J. Mech. Fluids, 13*, 387-399.

12. Nishioka, M. & Sato, H. (1978). Mechanism of determination of the shedding frequency of vortices behind a cylinder at low Reynolds numbers. *J. Fluid Mech., 89*, 49-60.

13. Norberg, C. (1994). An experimental investigation of the flow around a circular cylinder: influence of aspect ratio. *J. Fluid Mech., 258*, 287-316.

14. Dusek, J., Le Gal, P. & Fraunie, P. (1994). A numerical and theoretical study of the first Hopf bifurcation in a cylinder wake. *J. Fluid Mech., 264*, 59-80.

15. Jackson, C. P. (1987). A finite-element study of the onset of vortex shedding in flow past variously shaped bodies. *J. Fluid Mech., 182*, 23-45.

16. Huerre, P. & Monkewitz, P. (1987). Local and global instabilities in spatially developing flows. *Ann. Rev. Fluid Mech., 22*, 473-537.

17. Landau, L. &. Lifshitz, E. (1959). *Fluid mechanics, 6 course of theoretical physics*. Pergamon Press.

18. Stuart, J. (1971). Nonlinear stability theory. *Ann. Rev. Fluid Mech. 3*, 347-370.

19. Sohankar, A. (1996). *A numerical study of unsteady 2D flow around rectangular cylinders*. Publication No. 96/5, Dept. Thermo and Fluid Dynamics, Chalmers University of Technology, Gothenburg, Sweden.

20. Albarede, P. & Provansal, M. (1995). Quasi-periodic cylinder wake and the Ginzburg-Landau model. *J. Fluid Mech., 291*, 191-222.

21. Jeong, J. & Hussain, F. (1995). On the identification of a vortex. *J. Fluid Mech., 285*, 69-94.

22. Hunt, J. C. R., Wray, A. & Moin, P. (1988). Eddies, stream, and convergence zones in turbulent flows. *Centre of Turbulence Research Report CTR-S88*, 193.

23. Park, J., Kwon, K. & Choi, H. (1998). Numerical solutions of flow past a circular cylinder at Reynolds number up to 160, *KSME International Journal*, 1200-1205.

24. Franke, F., Rodi, W. & Schonung, B. (1990). Numerical calculation of laminar vortex shedding flow past cylinders. *J. of Wind Engineering Aerodynamics, 35*, 237-257.

25. Zhang, J. & Dalton, C. (1998). A three-dimensional simulation of a steady approach flow past a circular cylinder at low Reynolds number. *I. J. for Numerical Methods in Fluids, 26*, 1003-1022.

26. Rosenfeld, M. (1994). Grid refinement test of time-periodic flows over bluff bodies. *Computers Fluids, 23*, 693-709.

27. Norberg, C. (2003). *Fluctuating lift on a circular cylinder: review and new measurements. J. of Fluids and Structures, 17*, 57-96.

28. Braza, M., Chassaing, & Minh, H. (1986). Numerical study and physical analysis of the pressure and velocity fields in the near wake of a circular cylinder. *J. Fluid Mech., 165*, 79-130.

www.SID.ir